RSC Advances

PAPER

View Article Online
View Journal | View Issue



Cite this: *RSC Adv.*, 2020, **10**, 43870

# Comprehensive DFT investigation of transition-metal-based new quaternary Heusler alloys CoNbMnZ (Z = Ge, Sn): compatible for spin-dependent and thermoelectric applications†

Ab Quyoom Seh and Dinesh C. Gupta *

The hunt for high spin polarization and efficient thermoelectric materials has endured for decades. In this paper, we have explored the structural, mechanical stability, magneto-electronic, and thermoelectric properties of two new quaternary Heusler alloys, CoNbMnZ (Z = Ge, Sn), using first-principles simulation methods. The alloys are stable, showing a $Y_1$-type phase and ferromagnetic nature. Based on a generalized gradient approximation method, the alloys exhibit metallic nature; upon employing a modified version of the Becke–Johnson potential, both alloys demonstrate half-metallic nature, with gaps of 0.43 and 0.45 eV, which is a precursor for high spin polarization in these alloys. The alloys also follow the necessary Slater–Pauling rule condition $M_T = Z_T - 24$ for half-metallicity and they have a total magnetic moment of 1 $\mu_B$. Elastic parameters convey the mechanical stabilities of these alloys, with Debye temperatures of 518 K and 445 K. These materials act as anisotropic media with respect to longitudinal and transverse sound velocities. Possible energy efficiency and thermoelectric applications were scrutinized *via* computing Seebeck coefficients, electrical and electronic lattice thermal conductivities, and, lastly, power factors. The highest *S* values for Ge- and Sn-based alloys are 60.43 and 68.2 μV $K^{-1}$, respectively, and the highest power factors are 32 and 35 μW $K^{-2}$ $cm^{-1}$, respectively, suggesting potential efficient applications in thermoelectric power generation.

Received 18th September 2020
Accepted 2nd November 2020

DOI: 10.1039/d0ra08007a

rsc.li/rsc-advances



## Introduction

In recent decades, Heusler alloys have captured a lot of attention due to their possible utilization in various technologies, like spintronics,[1–4] giant magnetoresistance devices,[5] shape memory alloys,[6] and thermoelectric devices.[7,8] This is because these alloys are mostly ferromagnetic with high Curie temperatures.[9,10] Heusler alloys also exhibit unique behavior at the Fermi level, with half-metallicity, giving rise to 100% spin polarization.[1,2,11] The high spin polarized currents make them suitable for enhancing the performances and properties of conventional semiconductor devices. These materials can be incorporated into spin filters, and spin-injection and magneto-optical devices.[12,13] The investigation of such materials has gained the interest of researchers, and a large number of theoretical and experimental studies have been carried out to find new materials with fascinating properties. Besides the many variants of Heusler alloys, recently, new materials called quaternary Heusler alloys are being investigated thoroughly. To date, a large number of such alloys has been investigated both theoretically and experimentally.[1,2,13–16] Among these alloys, Co-based examples are of particular interest due to their high Curie temperatures and high spin polarization at the Fermi energy ($E_F$), making them prospective candidates for use in spin-dependent devices.[17] These materials can also find applications as energy-conserving materials.[18,19]

According to statistical results, a significant percentage (more than 60%) of energy is lost as waste heat throughout the world. The depletion of energy resources and degradation of the environment have forced the scientific world to find alternative efficient and eco-friendly energy technologies. The disastrous consequences emerging from the combustion of fossil fuels have caused severe problems to human health and energy reservoirs due to environmental pollution and energy wastage. Hence, the search for energy-efficient and eco-friendly materials is currently a vital challenge globally.[20] One of the fundamental solutions to such problems is the concept of thermoelectricity, which enables the direct conversion of heat energy into electrical energy. Thermoelectric devices do not require any environmentally harmful fluids like chlorofluorocarbons or fullerenes, nor do they release harmful gases into environment; for this reason, these are called green-energy materials.[21] Heusler compounds have been found to be compatible for

*Condensed Matter Theory Group, School of Studies in Physics, Jiwaji University, Gwalior-474011, India. E-mail: sosfizix@gmail.com*

† Electronic supplementary information (ESI) available. See DOI: 10.1039/d0ra08007a

converting dissipated heat into electric energy.[22] These compounds are providing new sustainable energy technology approaches to overcome energy crises.

As mentioned above, a huge number of quaternary Heusler alloys have been investigated that exhibit fascinating properties. Their high spin polarization, compatible lattice structures, and high thermoelectric efficiency with conventional half-metallic ferromagnetism have inspired us to design new quaternary Heusler half-metallic CoNbMnZ (Z = Ge, Sn) alloys. Since no experimental or theoretical information is available about these alloys, we performed detailed analysis, which is vital for understanding the structural, mechanical stability, strength, and natural properties of these material for experimental synthesis and technological applications. The authenticity of the results for these alloys can be confirmed *via* comparing the obtained results with other Heusler alloy families, especially with the nearest-neighbor family CoX′NbGa (X = Cr, Mn, Fe).[23] We will also explore how the results are dependent on electron correlations in the narrow d-bands of transition-metal atoms.

## Methodology

Calculations of total energies and electronic properties were done using DFT. The aforementioned alloys were analyzed by utilizing Wein2k simulation code based on the full-potential linearized augmented plane wave method (FP-LAPW). The solutions to Kohn–Sham equations are obtained through an iterative method. Since the exchange–correlation potentials are not exactly known, we have employed two different methods, the Perdew–Burke–Ernzerhof generalized gradient approximation (GGA-PBE) and integrated modified Becke–Johnson GGA (GGA + mBJ) methods.[24,25] Highly correlated electron systems, including transition metal (TM) complexes that possess d- and f-states, are not effectively estimated *via* the GGA method. The modified Becke–Johnson method is used to overcome erroneous estimated values when using the GGA method. To restrict the number of plane-waves, a cut-off parameter of $R_{MT}K_{MAX} = 6$ has been employed, where the former represents the largest reciprocal lattice vector and the latter is the smallest muffin tin sphere radius. For Brillouin zone (BZ) integration, a tetrahedral method following Monkhorst–Pack conventions with a dense *k*-mesh of 3000 points has been used. The $R_{MT}$ values of Co, Nb, Mn, and Ge are chosen in such a way as to prevent charge leakage to the interstitial region and, thus, total energy convergence is also ensured. The energy and charge convergence criteria are set to $10^{-7}$ e nm$^{-1}$ and $10^{-4}$ e, respectively, so as to ensure that the self-consistent calculations are accurate and fully converged.

In order to calculate the transport properties of the compounds, BoltzTraP2 code[26] using constant relaxation time approximations for the charge carriers is employed. This approximation is based on the fact that these parameters do not vary readily with energy on the $k_BT$ scale.[27] The electrical conductivity ($\sigma$), electronic thermal conductivity ($\kappa_e$), and Seebeck coefficient ($S$) values can be determined through the following relationships:[28]

$$S = \frac{eK_B}{\sigma}\int\left(\frac{-\partial f_0}{\partial E}\right)\frac{\varepsilon-\mu}{K_BT}\Xi(\varepsilon)\mathrm{d}\varepsilon$$

$$\sigma = \int\left(\frac{-\partial f_0}{\partial E}\right)\Xi(\varepsilon)\mathrm{d}\varepsilon$$

$$\kappa_e = {k_B}^2T\int\left(\frac{-\partial f_0}{\partial E}\right)\left(\frac{\varepsilon-\mu}{K_BT}\right)^2\Xi(\varepsilon)\mathrm{d}\varepsilon$$

$$\Xi^{\alpha,\beta}(\varepsilon) = \sum_K \delta(\varepsilon-\varepsilon_K)v_K^\alpha v_K^\beta \tau_K$$

where $v_K^\alpha$ depicts the $\alpha$ component of the group velocity with the wave vector $k$.

To determine the transport coefficients, a large *k*-point mesh of 150 000 $k$ points was used in order to obtain more precise results.

### Structural

The crystal framework associated with the *XX′YZ* quaternary Heusler alloys consists of four interpenetrating fcc lattices with the space group $F\bar{4}3m$. The prototype structure of these alloys is LiMgPdSn-type, which is also called a Y-type structure. The structural description of an *XX′YZ* alloy is such that the atom *X*

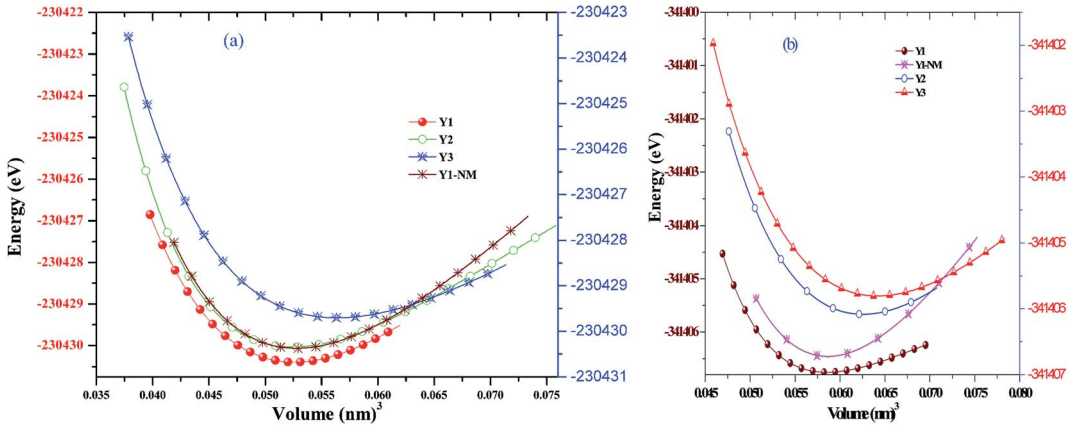


Fig. 1 Energy optimization curves of CoNbMnZ ((a) Ge, (b) Sn) in different phases.

Table 1 Equilibrium parameters, *viz.* volume ($nm^3$), bulk modulus ($B$, GPa), derivative of bulk modulus ($B'_0$), ground state energy ($E_0$, eV), and relaxed lattice constant ($a$, nm) of CoNbMnGe and CoNbMnSn alloys with different structure types

| | Phase | $V$ | $B$ | $B'_0$ | $E_0$ | $a$ |
|---|---|---|---|---|---|---|
| CoNbMnGe | $Y_1$ | 0.05257 | 225.46 | 4.24 | −230430.39230 | 0.614 |
| | $Y_1$-NM | 0.05282 | 216.63 | 4.51 | −230430.37695 | 0.590 |
| | $Y_2$ | 0.05246 | 197.38 | 5.95 | −230430.34900 | 0.614 |
| | $Y_3$ | 0.05633 | 149.50 | 5.04 | −230429.70450 | 0.621 |
| CoNbMnSn | $Y_1$ | 0.5923 | 145.33 | 5.24 | −341406.75163 | 0.6257 |
| | $Y_1$-NM | 0.05865 | 197.33 | 4.55 | −341406.72558 | 0.6142 |
| | $Y_2$ | 0.05633 | 149.76 | 4.79 | −341406.084796 | 0.6216 |
| | $Y_3$ | 0.06415 | 129.75 | 4.50 | −341405.806459 | 0.6301 |

with the most valance electrons occupies the 4*c* site of the lattice. The sp atom *Z* will occupy the 4*a* position, and *X*′ and *Y* are placed at the 4*b* and 4*d* positions, respectively. Two types of interactions, *viz* ionic and covalent, occur in a Heusler-type structure. This is because the 4*a* and 4*c* sites of the unit cell form a ZnS-type lattice, and the bonding between the atoms has covalent nature. The sites 4*a* and 4*b* form an octahedron with NaCl-type structure, and the interactions among the atoms have strong ionic character.[29] Thus, overall, quaternary Heusler alloys depict polar covalent bonding character.

Depending upon the occupancy of atoms in the unit cell, there are three inequivalent possible structural types. The occupancy of Wyckoff positions in the $Y_1$ phase is $X$ = (0.75, 0.75, 0.75), $X'$ = (0.50, 0.50, 0.50), $Y$ = (0.25, 0.25, 0.25), and $Z$ = (0, 0, 0). For the $Y_2$ and $Y_3$ phases, the atoms are situated at $X$ = (0.25, 0.25, 0.25), $Y$ = (0.50, 0.50, 0.50), $X'$ = (0.75, 0.75, 0.75), and $Z$ = (0, 0, 0), and $X$ = (0.50, 0.50, 0.50), $Y$ = (0.75, 0.75, 0.75), $X'$ = (0.25, 0.25, 0.25), and $Z$ = (0, 0, 0), respectively.[30] These structural configurations are shown in Fig. S1(a–c) in the ESI.†

The physical properties (structural, electronic, magnetic, and transport) are greatly affected if there is any structural disorder or distortion; for this reason, we perform structural optimization in all possible phases. Structural optimization has been carried out to calculate the total energy and lattice constants, and to find the stable or ground state of the material *via* varying the unit-cell volume. Energy *vs.* volume curves are plotted in Fig. 1(a and b). From the plots it is evident that $Y_1$ has the least energy and, hence, is the most stable phase, and it is also the most stable phase for other similar CoX′NbGa (X = Cr, Mn, Fe) alloys.[23] The large energies in the $Y_2$ and $Y_3$ phases are attributed to the changing positions of atoms. In CoNbMnZ (Z = Ge, Sn) alloys, since Co is the atom with the maximum number of valence electrons, it will occupy the 4*c* (1/4, 1/4, 1/4) site. The p-block element Z has four outermost electrons and is the most electronegative atom in the present alloy, so it will occupy the 4*a* (0, 0, 0) site. Similarly, the third and fourth atoms (Mn, Nb) have seven and five valence electrons, respectively, so they will take up the 4*b* (1/2, 1/2, 1/2) and 4*d* (3/4, 3/4, 3/4) sites of the unit cell. The resultant ordered structure is called a $Y_1$-type structure. The various equilibrium lattice parameters ($a$), bulk moduli ($B$), pressure derivative of bulk modulus ($B'_0$), and total energies in two magnetic states are presented in Table 1. The obtained lattice constants in the most stable phase for CoNbMnGe and CoNbMnSn are 0.614 and 0.625, respectively, which are comparable to the lattice constant of CoNbMnGa (0.596 nm).

## Electronic properties

The novel properties of a material directly stem from the crystal structure and the electronic band profile. The electronic properties can be analyzed using GGA and mBJ methods, and by incorporating a Hubbard term with GGA. We have scrutinized the spin-polarized band structures of CoNbMnZ (Z = Ge, Sn) alloys along high-symmetry Brillouin zone (BZ) directions *via* GGA and mBJ techniques. Fig. 2(a and b) depicts the band structures of both alloys obtained *via* GGA; it is evident from the plots that many energy levels make metallic intersections at the Fermi level in the spin-up channel, hence creating metallic character. However, in spin-down orientation, the Fermi level is deserted, except at the *X*-point of the BZ for CoNbMnGe and the

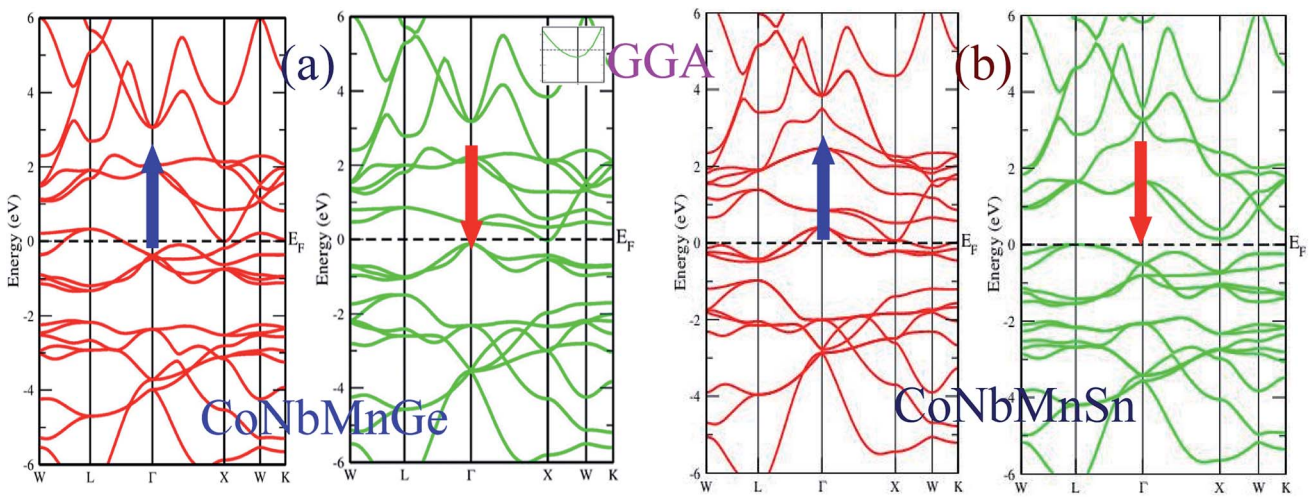


Fig. 2 Representations of the band structures of CoNbMnZ (Z = (a) Ge, (b) Sn) using the GGA approximation.

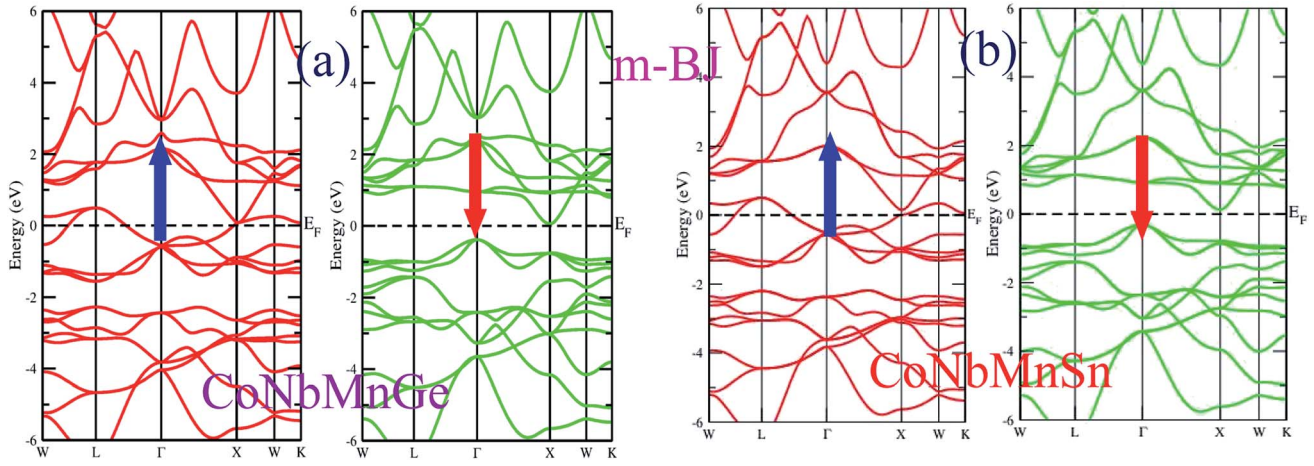


Fig. 3 The band structures of CoNbMnZ (Z = (a) Ge, (b) Sn) obtained *via* the mBJ method.

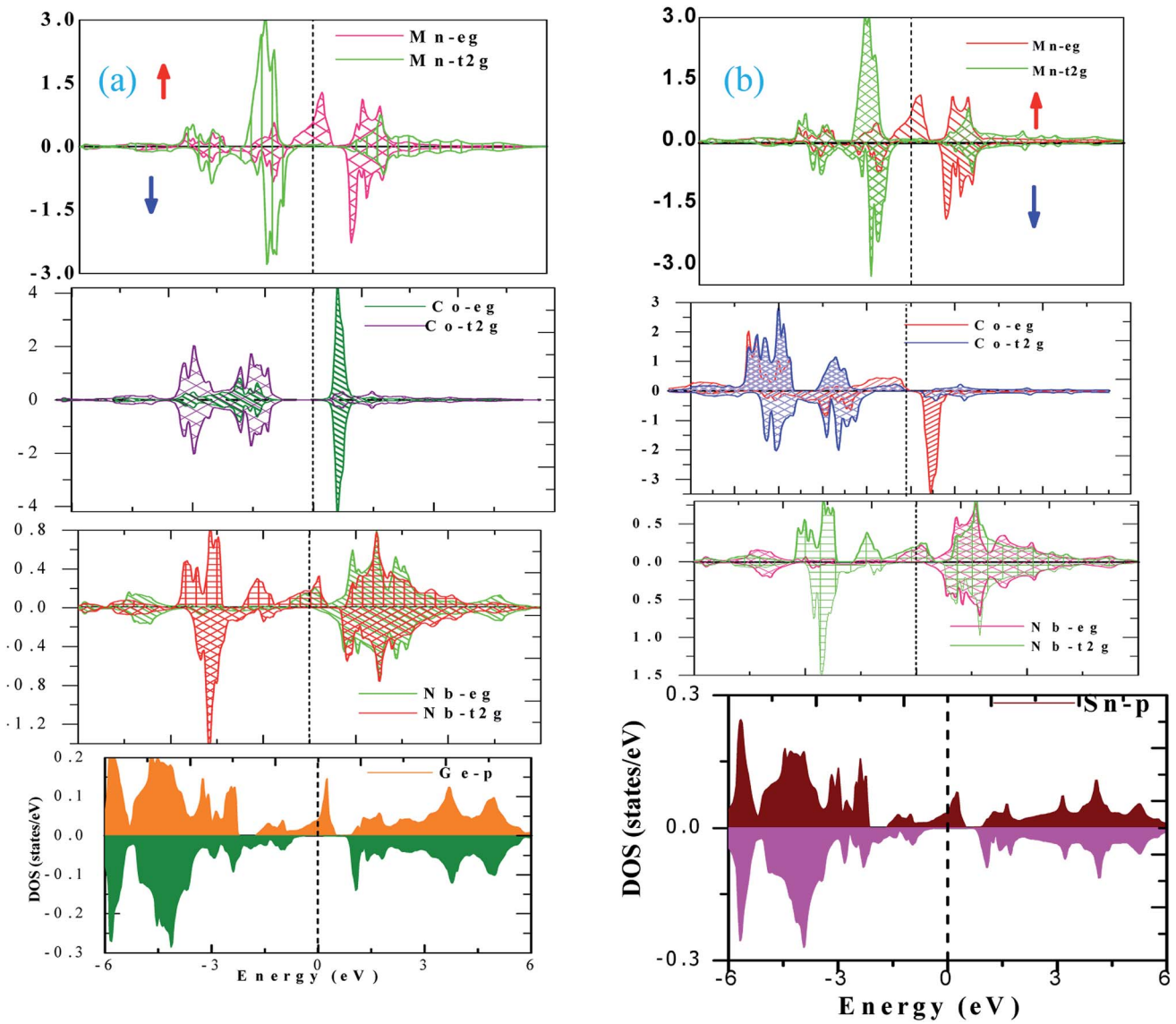


Fig. 4 The atom-resolved pDOS plots of both alloys ((a) Z = Ge; (b) Z = Sn) obtained using the mBJ method.

*L*-point of the BZ for CoNbMnSn. Upon zooming-in closely to the band structure, it is found that the energy band crosses the Fermi level, hence confirming the metallic character in the spin-down channel as well. Since the GGA method underestimates the band gap, we have incorporated the mBJ method into GGA in order to obtain the precise band structure. The mBJ band structure calculations are very effective compared to GGA. The elucidation of band structure using mBJ is presented in Fig. 3(a

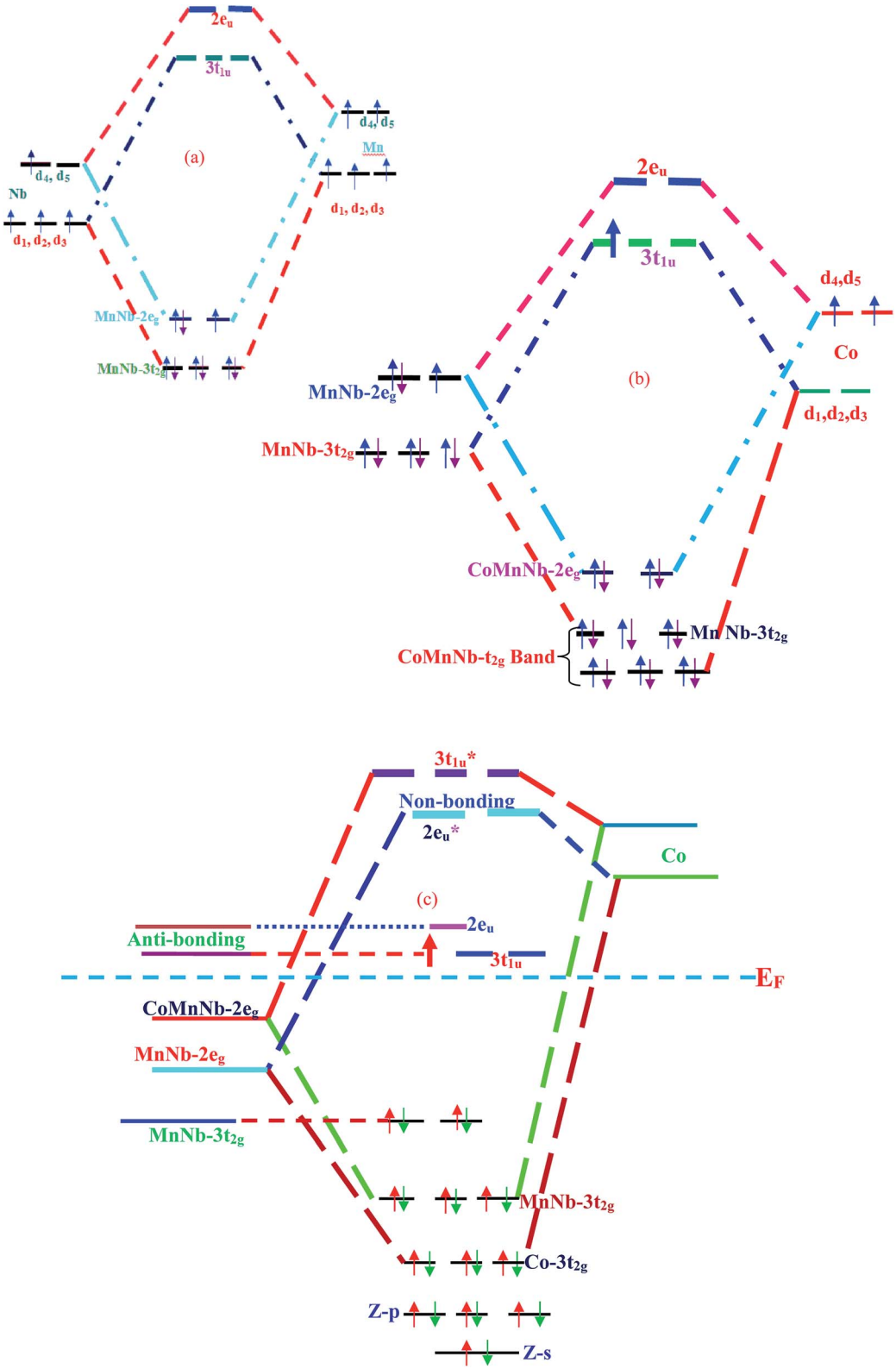


Fig. 5 (a) The hybridization of Mn–Nb. (b) The resultant hybridization of MnNb with Co. (c) The overall hybridization of the alloys.

 

and b). From the band plots it is evident that the energy states are crossing the Fermi level in the majority spin channel, indicating metallic character, whereas in the spin-down state, neither the valence nor conduction band touches the Fermi level, giving rise to half-metallic nature with indirect band gaps of 0.43 and 0.45 eV at the $\Gamma$ and $X$ points.

The electronic properties of CoNbMnZ (Z = Ge, Sn) alloys can be further explored *via* plotting partial density of states (pDOS). pDOS gives information about the energy states occupied in a particular energy interval. In order to find the contributions of atomic energy levels to the band structure, we have plotted the pDOS of CoNbMnZ (Z = Ge, Sn) using the GGA approximation, as shown in Fig. S5(a and b) [shown in the ESI].† From both plots it is obvious that many energy states make metallic intersections with the Fermi level in the spin-up channel. Upon observing the pDOS in the minority spin channel, it can be seen that some energy levels cross the Fermi level and, hence, the alloys exhibit metallic nature in the spin-down channel as well. Since GGA usually underestimates the band gap, we employed mBJ, and the pDOS plots obtained using the mBJ method are shown in Fig. 4(a and b) for both alloys in the different spin channels. From the figures it is obvious that the alloys are metals in the majority spin channel, whereas in the minority channel none of the energy levels exists at the Fermi level; hence, the alloys show perfect half-metallic character. The band structures and pDOS of CoX′NbGa (X = Cr, Mn, Fe) alloys also show half-metallic nature.

### Origin of the half-metallic gap

The origin of the half-metallic nature of CoNbMnZ (Z= Ge, Sn) can be explored *via* presenting the possible hybridization among the constituent atoms schematically. Transition metal atom d-states in the presence of a crystal field are decomposed into doubly degenerate $e_g$ ($d_{x^2-y^2}$, $d_{z^2}$) and triply degenerate $t_{2g}$ ($d_{xy}$, $d_{yz}$, $d_{zx}$) states. The appearance of a band gap in the minority spin state and the half-metallicity of the Heusler compounds originates from the d–d hybridization of transition metal atoms. In the present alloys, Z is the most electronegative element and Nb has an exceptional electronic configuration ($4d^4 5s^1$). Therefore, the s-state electrons, two from Mn and one from both Nb and Co, will be accumulated by Z to complete its octet and achieve a minimum energy state. Thus, Z makes a negligible contribution to the DOS in the neighborhood of the Fermi level. Considering the d–d hybridization of the Mn and Nb atoms, according to Jahn–Teller theory, the degeneracy of the d-orbitals is lifted due to their mutual interaction and the d states of each transition metal atom hybridize according to their symmetry; this creates five bonding ($2e_g$, $3t_{2g}$) and five anti-bonding ($2e_u$, $3t_{1u}$) orbitals.[31] Mn and Nb have five and four d-electrons, respectively. The possible orbital hybridization between the Mn and Nb d-states is profiled in Fig. 5(a). From the figure, it is evident that the MnNb-$3t_{2g}$ state is completely filled, hence the Mn and Nb bonding $3t_{2g}$ state lies wholly in the valence band and the corresponding anti-bonding state lies in the conduction band. The $2e_g$ state of MnNb has only three electrons, while Co has 8 electrons, 6 of which are in the $3t_{2g}$ state and 2 are in the $2e_g$ state, which may be due to s-Rydberg destabilization of a metal complex;[32] therefore, the $2e_g$ state of MnNb will couple with the Co-$2e_g$ state of Co, and this is depicted in Fig. 5(b). From the figure, it is obvious that the $2e_g$ state is completely paired; one electron remains unpaired and this unpaired electron occupies the $3t_{1u}$ state. The resultant hybridization is shown in Fig. 5(c); due to the intermixed character of the energy bands, both the Co and Mn-$e_g$ states lie in the valence band in the respective spin channels and their anti-bonding states lie in the conduction band. The unpaired electron in the $3t_{1u}$ state is responsible for the metallic nature of the alloy in the spin-up channel, 100% spin polarization, and the magnetic moment of 1 $\mu_B$ according to the Slater–Pauling rule.

### Electron density plots

Confirmation of the possible d–d hybridization of the materials under study is obtained *via* charge density plots and contour

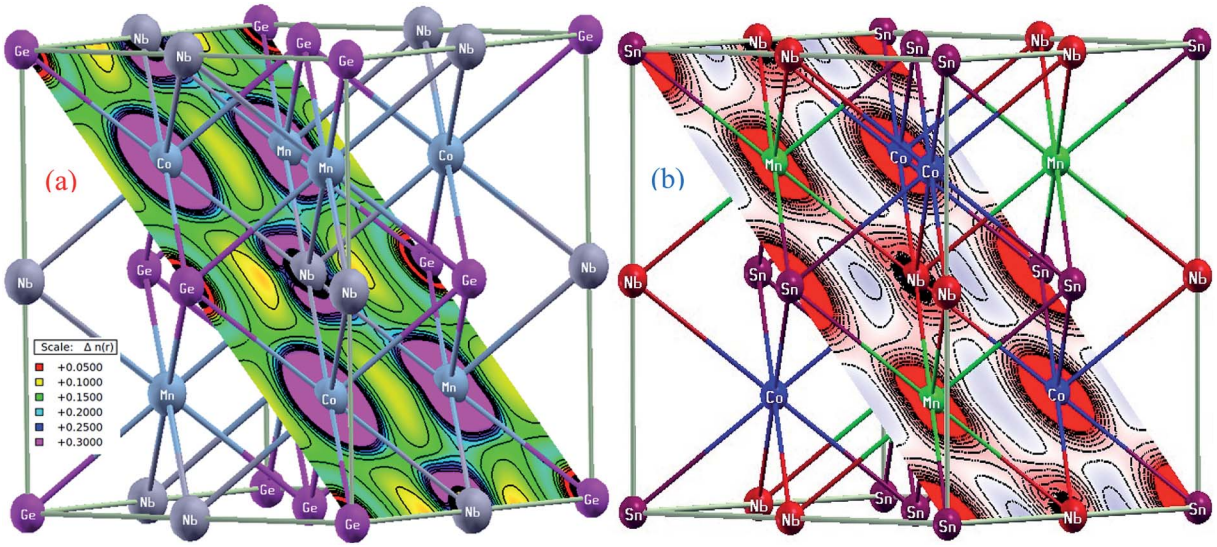


Fig. 6 Electron density plots of both alloys ((a) Z = Ge; (b) Z = Sn) along the ⟨111⟩ plane direction.

graphs, as portrayed in Fig. 6(a and b). Electron density plots play a vital role in the interpretation of the chemical and physical properties of a material based on electron clouds, hence denoting the nature of bond formation between different atoms. To obtain a clear perception of all atoms, we have chosen the ⟨110⟩ plane along the diagonal direction of the $C1_b$ structure.[33] It is clear from the plots that the shape of the charge density cloud of Nb is dumbbell-type along the Z-atom direction, indicating an ionic interaction. This may be due to the more electronegative character of Z compared with Nb. From these plots, it is also evident that the Co charge density is spherically symmetric, while the Mn density is nearly spherical, demonstrating that Co and Mn interact covalently, as is evident from the orbital hybridization diagram.

## Magnetic properties

The magnetic nature of a material can be described based on its total magnetic moment. Table 2 presents the absolute and individual magnetic moments of CoNbMnZ (Z = Ge, Sn) alloys using GGA and mBJ methods. The alloys follow the Slater–Pauling rule $M_T = Z_T - 24$, with a total magnetic moment of 1 $\mu_B$, which is an integral value, and, hence, the alloys are perfect half-metallic materials. $\mu_{int}$ describes the interstitial magnetic moment. From the table it is obvious that $\mu_{int}$ has almost zero value, and we can say that there is almost zero charge leakage to the interstitial regions of the alloys. The prominent contribution to the total magnetic moment comes from Co atoms. The contributions from the Z and Nb atoms to the magnetic moment are negligible in comparison to the Co and Mn atoms. The magnetic moments calculated *via* GGA and mBJ are almost same. Since the number of valence electrons is 25, there are 12 occupied states in both channels, while the extra electron is responsible for the magnetic moment and spin-polarization in the alloys. This can be further confirmed by examining the CoX′NbGa (X = Cr, Mn, Fe)[23] family of alloys, where the authors gave detailed descriptions of the magnetic moments of CoCrNbGa and CoFeNbGa and the zero magnetic moment of CoMnNbGa.[23]

## Cohesive energy

Theoretically, the stability of a material can be determined based on the cohesive energy ($E_{coh}$), mechanical stability and formation energy. The stability of a material can be correlated with its cohesive energy, which is defined as the energy required to split the material into its individual constituents, hence indicating the bond strength of a compound.[34] The cohesive energy, therefore, is a measure of the inter-molecular energy of a substance. The $E_{coh}$ values of the alloys under investigation can be calculated using the formula below, which involves the sum of the individual atomic energies minus the total energy of the compound:

$$E_{Coh} = \frac{(E_{Co} + E_{Nb} + E_{Mn} + E_Z) - E_{Tot}}{4}$$

where $E_{Co}$, $E_{Nb}$, $E_{Mn}$, and $E_Z$ are the energies of isolated atoms, and $E_{Tot}$ is the bulk energy of the considered material. The higher the cohesive energy value, the more stable the structure will be. The computed value of $E_{Coh}$ for CoNbMnGe is 5.43 eV per atom and it is 5.17 eV per atom for CoNbMnSn, affirming that the materials are stable.

Table 2 Atom-resolved magnetic moments

| Magnetic moment ($\mu_B$) | CoNbMnGe | | CoNbMnSn | |
|---|---|---|---|---|
| | GGA | mBJ | GGA | m-BJ |
| $\mu_{int}$ | −0.01 | −0.04 | 0.03 | −0.06 |
| $\mu_{Co}$ | 0.44 | 0.46 | 0.44 | 0.45 |
| $\mu_Z$ | 0.02 | 0.07 | −0.05 | −0.03 |
| $\mu_{Nb}$ | 0.19 | 0.14 | 0.24 | 0.25 |
| $\mu_{Mn}$ | 0.34 | 0.37 | 0.39 | 0.39 |
| $\mu_{Tot}$ | 0.98 | 1.0 | 0.99 | 1.0 |

## Mechanical properties

The mechanical properties of a material define its ability to regain and recover its original configuration after the cessation of stress. Elastic constants ($C_{ij}$) are indispensable for exploring the mechanical properties of materials. These properties determine the favorable conditions for initiating and retaining the quality of the crystal structure. The mechanical constants are linked to some thermodynamic parameters, like specific heat, the Debye temperature, and the Gruneisen parameter. Elastic properties fundamentally determine the mechanical strength of a material, for example, the fracture toughness, sound velocity, load deflection, thermoelastic stress, and, indirectly, the melting temperature, which are basic requirements for determining technologically favorable materials. Most importantly, these parameters provide valuable information regarding the nature of the forces exerted on atoms and the bonding and stiffness of the material. For cubic crystals, only three independent elastic tensor components are needed, they are $C_{11}$, $C_{12}$, and $C_{44}$. The first represents unidirectional squeezing along the principal crystallographic directions. $C_{11}$ undergoes a large change because the volume change is very sensitive to temperature and pressure variations. The constants $C_{12}$ and $C_{44}$ determine resistance to shear deformation and are linked to elasticity of shape, which is a shear constant. Transverse strain or shear causes deformation without a change in volume. Thus, $C_{12}$ and $C_{44}$ are expected to be less sensitive to temperature and pressure compared with $C_{11}$.

Once these elastic constants are obtained, the elastic behavior can be studied *via* calculating other elastic parameters, shear ($G$) and bulk modulus ($B$), which are calculated through the Voigt–Reuss–Hill approximation.[35,36]

Some other important elastic parameters, such as Poisson's ratio ($\nu$), anisotropic factor ($A$), and Young's modulus ($E$), can be calculated using the following relationships:[37]

$$E = \frac{9BG}{3B + G};$$

$$\sigma = \frac{3B - 2G}{2(3B + G)};$$

$$A = \frac{2C_{44} + C_{12}}{C_{11}}$$

 

The magnitude of the resistance of a material when its volume is changed is defined through $B$, while the limit of the occurrence of plastic deformation upon shear stress is measured through the shear modulus. The values obtained for $\nu$, $B$, and $G$ from the alloys are given in Table 3. The values of bulk and shear modulus are positive, which is a true indication of the structural stability of the materials. The stiffness of a material depends on $Y$. The higher the value of $Y$, the stiffer a material will be. Pugh proposed the index of ductility ratio ($B/G$), which is also called Pugh's ratio, which characterizes the plastic behavior of a compound. The critical value of $B/G$ is 1.75. This is one of the most important and fundamental ratios that determines whether a material will show a brittle or ductile nature. If the ratio is greater than 1.75, the material shows ductile behavior, otherwise it shows a brittle nature.[38] The calculated value of $B/G$ for CoNbMnGe is 2.24 and it is 2.14 for CoNbMnSn, indicating that the materials possess ductile natures. This can also be confirmed from Cauchy's pressure: $C' = C_{12} - C_{44}$. A positive $C'$ value for a material corresponds to ductility, while a negative value of $C'$ indicates a brittle nature. For CoNbMnZ (Z = Ge, Sn) the values of $C'$ are positive, hence showing ductile natures.

The Poisson coefficient is a dimensionless parameter that provides good insight into the behavior of a material and the characteristics of the bonding forces existing within the material. The limiting values of this coefficient are 0.25 and 0.5, describing the lower and upper limits for central forces to exist within the constituents of an alloy. The value of $\nu$ is 0.1 for covalent compounds. For ionic and metallic bonding, the values are 0.25 and 0.33, respectively. We know that both ionic and covalent interactions exist in the $C1_b$ unit cell of a quaternary Heusler alloy. The computed Poisson ratio value for the CoNbMnGe alloy is 0.30 and it is 0.29 for CoNbMnSn, suggesting that the metallic bonding nature is dominant. Furthermore, $\nu$ can also be used to determine whether a compound has a brittle or ductile nature, because the value of this ratio depends on the nature of bonding and is different for different materials (it varies in different materials). If the Poisson ratio is less than 0.25, then the material will exhibit a brittle nature. The values of $\nu$ for the alloys under investigation is greater than 0.25 indicating these materials are ductile in nature.

The Zener anisotropy factor plays an important role when examining the extent of isotropy of a material. It is denoted by $A$ and is defined in terms of lattice constants. For a perfect isotropic material, the value of $A = 1$ (unity). If the value of $A$ deviates from unity (either greater or smaller), then the material possesses anisotropy. When the mechanical properties of a material alter along different directions then it is said to be an anisotropic material. A high value of elastic anisotropy in a material is associated with the chance of micro-cracks arising in a compound. Since the alloys exhibit high anisotropy, the velocities of transverse and longitudinal waves will be different along different directions. These waves propagate along three different modes: one longitudinal and two transverse modes. The calculated values of these modes along different directions are presented in Tables 4 and 5.

Table 4 Calculated sound velocity ($v_t$, $v_l$, $v_m$; m s$^{-1}$), Debye temperature ($\theta_D$, K), and anisotropy ($A$) values

| Parameter | $v_t$ | $v_l$ | $v_m$ | $\theta_D$ | $A$ |
|---|---|---|---|---|---|
| CoNbMnAs | 3886 | 6403 | 4479 | 518 | 1.93 |
| CoNbMnSb | 2780 | 5170 | 3660 | 445 | 1.12 |

### Thermoelectric properties

The thermoelectric properties were elucidated using semi-classical Boltzmann transport theory. Thermoelectric materials provide an alternate approach for power generation and refrigeration. These materials can also act as heat pumps or solid-state refrigerators that do not use any moving parts. The performance of a thermoelectric material is governed by a dimensionless figure of merit, which is defined as $ZT = \frac{S^2\sigma T}{\kappa_e + \kappa_l}$, where the terms have their usual meanings.[39] Thermoelectric transport measurements, coupled with microstructure studies and theoretical modeling, show that the $ZT$ improvement is the result of low lattice thermal conductivity due to increased phonon scattering by grain boundaries and structural defects.

### Electrical conductivity

The variations of electrical conductivity $\sigma$ are shown in Fig. 7(a and b). It is evident from the plots that $\sigma$ decreases with temperature in the majority spin channel, which infers the metallic nature of the materials. Since the electrical conductivity of a metal is given by the equation $\sigma = ne\mu$, $\sigma$ depends on the concentration and mobility of carriers. As the value of '$e$' is constant and '$n$' is almost independent of temperature in metals, the decreasing trend can be attributed to the mobility behavior in the material. The values of $\sigma$ at 50 K are $8.0 \times 10^5$ W $\Omega^{-1}$ m$^{-1}$ and $7.73 \times 10^5$ W $\Omega^{-1}$ m$^{-1}$, which decrease with temperature and reach minimum values of $7.56 \times 10^5$ W $\Omega^{-1}$ m$^{-1}$ and $7.17 \times 10^5$ W $\Omega^{-1}$ m$^{-1}$ at 900 K in the spin-up channels of the alloys. As the alloys are semiconducting in the spin-down channel and the conductivity of a semiconductor is given by the equation $\sigma = n_i|e|(\mu_e + \mu_h)$, with a rise in temperature, the concentration of carriers '$n_i$' increases due to the transition of

Table 3 Obtained and computed mechanical parameters

| Alloy | $C_{11}$ | $C_{12}$ | $C_{44}$ | $B_V$ | $B_R$ | $B$ | $G_V$ | $G_R$ | $G$ | $Y$ | $\nu$ | $C_P$ | $B/G$ |
|---|---|---|---|---|---|---|---|---|---|---|---|---|---|
| CoNbMnGe | 306.05 | 162.46 | 138.37 | 210.32 | 210.32 | 210.32 | 111.74 | 75.88 | 93.81 | 245.01 | 0.30 | 24.09 | 1.93 |
| CoNbMnSn | 251.62 | 103.41 | 83.36 | 152.81 | 152.81 | 152.81 | 79.65 | 62.72 | 71.18 | 184.84 | 0.29 | 20.05 | 1.12 |

Table 5 Velocities (m $s^{-1}$) of elastic waves along different directions for CoNbMnZ (Z = Ge, Sn)

| Propagation direction | Mode of vibration | $C_{eff}$ | CoNbMnGe | CoNbMnSn |
|---|---|---|---|---|
| [100] | $v_l$ | $C_{11}$ | 6110 | 5220 |
| | $v_{t1}$ | $C_{44}$ | 4112 | 3010 |
| | $v_{t2}$ | $C_{44}$ | 4112 | 3010 |
| [110] | $v_l$ | $(C_{11} + C_{12} + 2C_{44})/2$ | 6749 | 5310 |
| | $v_{t1}$ | $C_{44}$ | 4112 | 3010 |
| | $v_{t2}$ | $(C_{11} - C_{12})/2$ | 3000 | 2830 |
| [111] | $v_l$ | $(C_{11} + 2C_{12} + 4C_{44})/3$ | 6947 | 5344 |
| | $v_{t1}$ | $(C_{11} - C_{12} + C_{44})/3$ | 3889 | 2890 |
| | $v_{t2}$ | $(C_{11} - C_{12} + C_{44})/3$ | 3889 | 2890 |

electrons from the valence to the conduction band. The magnitude of $\mu_e + \mu_h$ will decrease with an increase in temperature, but this decrease will not overcome the increasing trend of $n_i$; hence, the conductivity increases. The values of $\sigma$ in the spin-down channels increase, and maximum values of 0.07 $\times 10^5$ W $\Omega^{-1}$ $m^{-1}$ and 0.42 $\times 10^5$ W $\Omega^{-1}$ $m^{-1}$ are attained at 900 K, hence signifying the semiconducting nature of the alloys.

### Thermal conductivity

One of the conditions that a promising thermoelectric material must meet is that the thermal conductivity should be as low as possible. The lower the value of $\kappa_e$, the more thermo-efficient the material will be. The variations of electronic thermal conductivity with temperature are plotted in Fig. 8(a and b). From the plots it is obvious that $\kappa_e$ shows an increasing trend in both spin channels. It can be seen from the graphs that the variation of $\kappa_e$ in the majority spin state is greater compared to the spin-down channel. This can be attributed to interactions between the carriers and the anisotropy of lattice forces. The values of $k$ at room temperature in the spin-up state are 0.0197 W $m^{-1}$ $K^{-1}$ and 0.093 W $m^{-1}$ $K^{-1}$ and these increase linearly to maximum values of 3.37 W $m^{-1}$ $K^{-1}$ and 1.59 W $m^{-1}$ $K^{-1}$ at 900 K. The $k$-values in the minority spin state at room temperature are 0.010 W $m^{-1}$ $K^{-1}$ and 0.002 W $m^{-1}$ $K^{-1}$; a nonlinear trend is seen, and peak values of 0.755 W $m^{-1}$ $K^{-1}$ and 0.3833 W $m^{-1}$ $K^{-1}$ are obtained at 900 K. The small increase of $\kappa_e$ is due to the semiconducting nature of the alloys in the spin-down state.

### Seebeck coefficient

The variations of the Seebeck coefficient in the spin-up channels for CoNbMnZ (Z = Ge, Sn) are depicted in Fig. 9. The values of $S$ in the entire temperature range are positive in both spin channels, signifying the presence of holes as majority carriers. It is clear from the plots that $S$ increases with an increase in

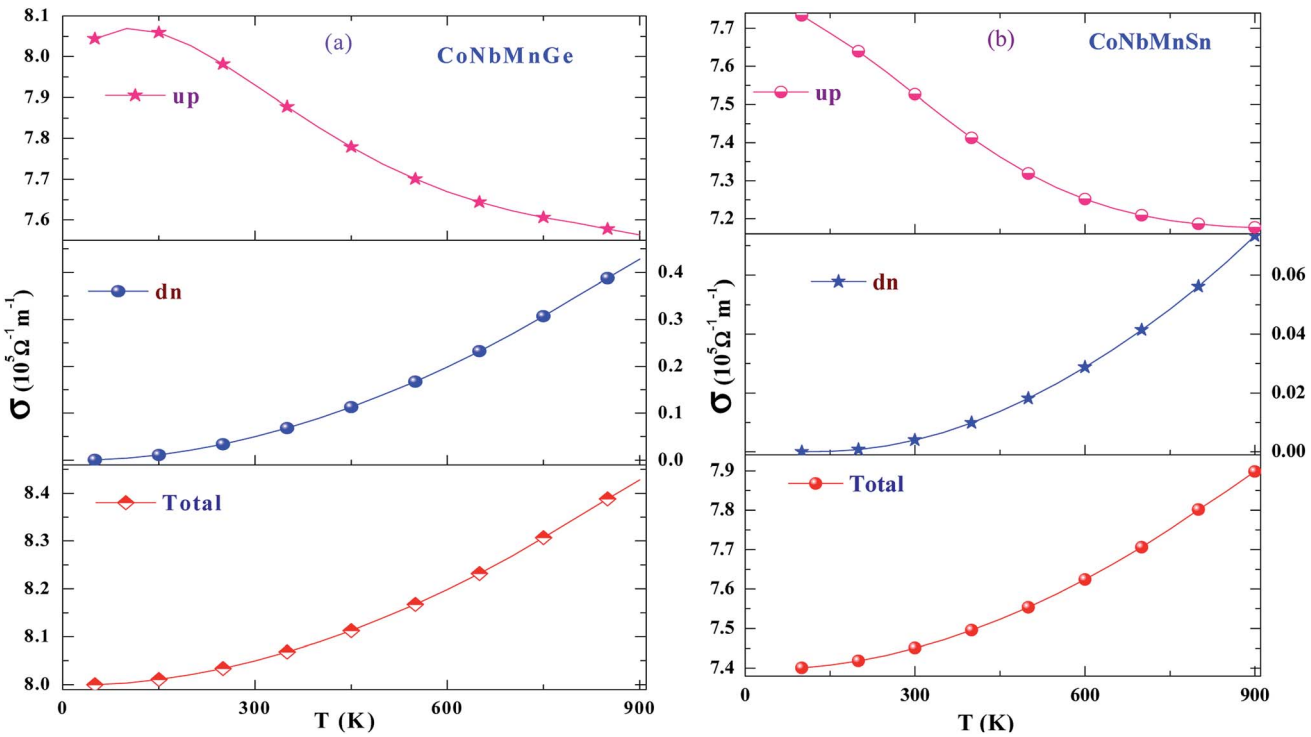


Fig. 7 The variation of electrical conductivity with temperature for CoNbMnZ (Z = (a) Ge, (b) Sn) alloys.

 

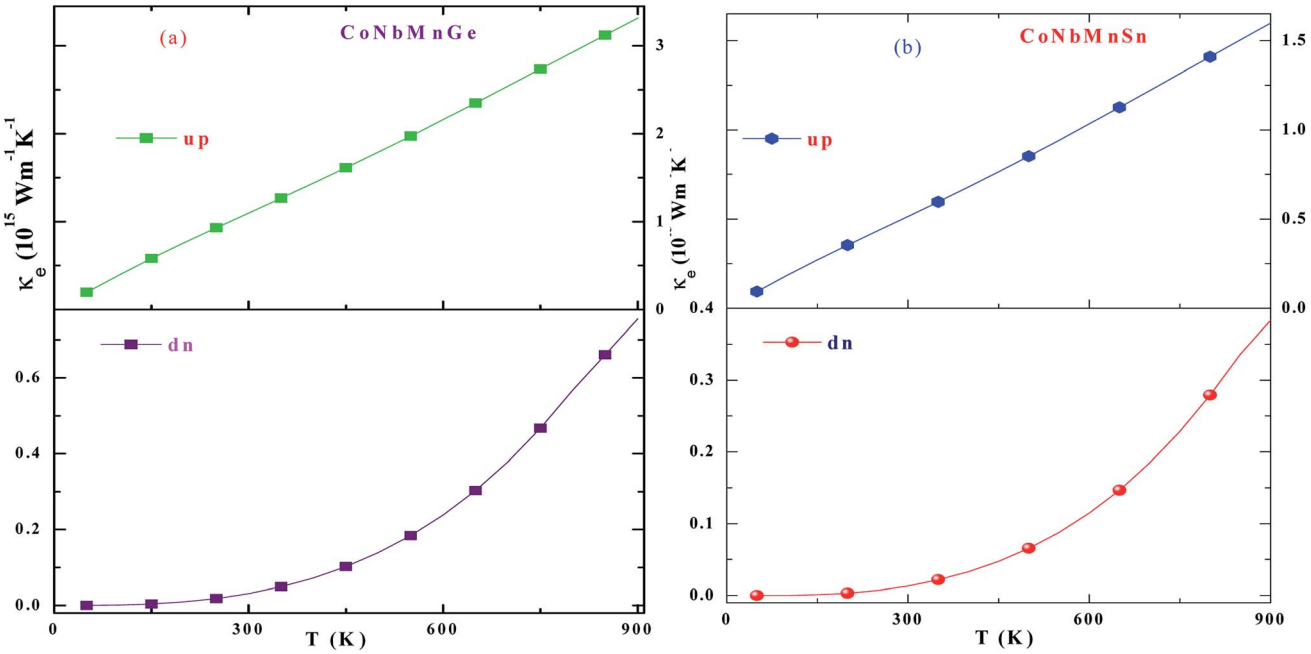


Fig. 8 The change in electronic thermal conductivity of CoNbMnZ (Z = (a) Ge, (b) Sn) alloys with temperature.

temperature, from 7.68 and 8.93 at 50 K to 62.45 and 70.55 at 900 K in the majority spin channels of both alloys. The variations of $S$ in the minority spin channels are profiled in Fig. 10. As the materials are semiconducting in the spin-down channels, they have minimum carrier concentrations at lower temperatures. The Seebeck coefficient has an inverse relation with carrier concentration ($n$), as shown in the equation:

$$S = \frac{8\pi^2 k^2}{3e\hbar^2} m^* T \left(\frac{\pi}{3n}\right)^{\frac{2}{3}}.$$

Hence, maximum values are seen at very low temperatures. As the temperature is increased, the electrons in the valence band obtain sufficient energy to be excited into the conduction band, creating electron–hole pairs; due to this, the carrier concentration increases gradually. Hence, this results in a decrease of $S$ in the minority spin channels. From the figure, it is evident that the values of $S$ in the spin-down channels at 50 K are 471.25 and 767.50; these values decrease readily with temperature and attain minimum values of 120.72 and 53.20 at 900 K for the alloys. The total $S$ value is determined using the two current model. The total thermopower is the average value of Seebeck coefficients from both spin configurations, weighted based on their corresponding conductivities. The variations of the total S values are plotted in Fig. 11; it is evident that the value of $S$ increases from 50–900 K and achieves maximum

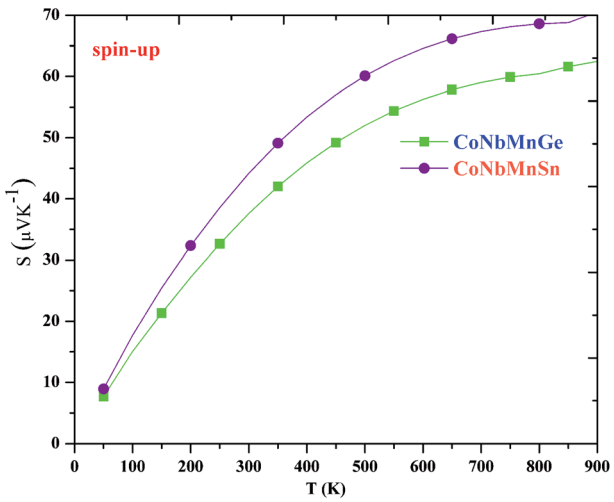


Fig. 9 Seebeck coefficients in the spin-up channel.

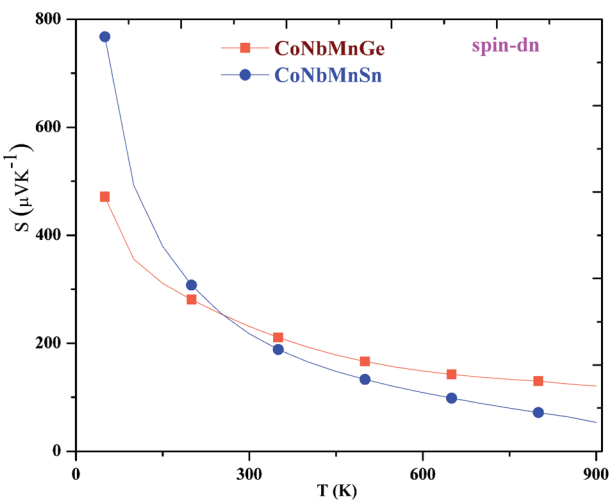


Fig. 10 Seebeck coefficients in the spin-down channel.

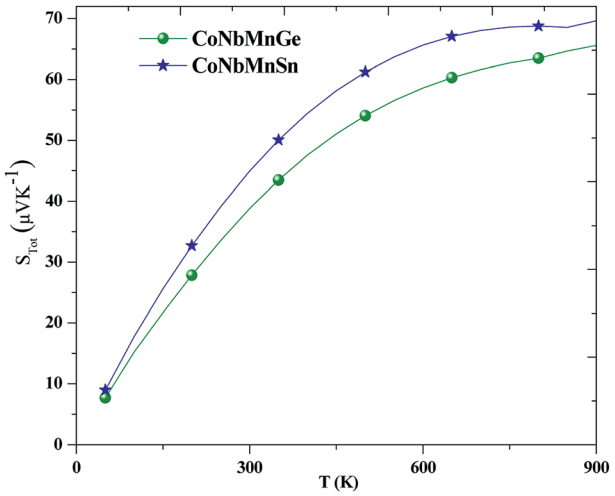


Fig. 11 The change in the total Seebeck coefficient with $T$ (K).

values of 65.57 and 69.62. The thermoelectric parameters follow the same trend as shown by CoX′NbGa (X = Cr, Mn, Fe) alloys.

The power factor (PF) of a material is determined by a weighted average of the Seebeck coefficient and the total electrical conductivity, *i.e.*, PF=$S^2\sigma$. It describes the efficiency of a material, and a high value of PF implies higher efficiency. The variations of the PF are depicted in Fig. 12 for both alloys. It is evident from the plots that the PF increases with temperature and reaches maximum values of 32 and 35.

To further confirm the relevance, we compare the pDOS, band structures, and thermoelectric parameters and study whether they follow the same trend. The band structure and DOS plots shown in Fig. 1–4 convey CoNbMnZ (Z = Ge, Sn) to be half metallic with metallic character in the majority spin channel. Upon analyzing the electric conductivity and Seebeck coefficients, we observe that electric conductivity decreases with temperature, while the Seebeck coefficient increases, in the spin-up channel of CoNbMnZ (Z = Ge, Sn) (see Fig. 6 and 8). Since these behaviors of $\sigma$ and $S$ are a peculiar characteristic of metals, this confirms that CoNbMnZ (Z = Ge, Sn) behaves as a metal in the majority spin channel. However, in the spin-down channel of CoNbMnZ (Z = Ge, Sn), the reverse effect is observed, *i.e.*, $S$ decreases while $\sigma$ increases, suggesting the semiconducting nature in this spin orientation. Thus, in a nutshell, it can be concluded that both the band structures and thermoelectric properties suggest the half-metallic character of CoNbMnZ (Z = Ge, Sn). The resemblance in results between the electronic and transport properties authenticates our investigation.

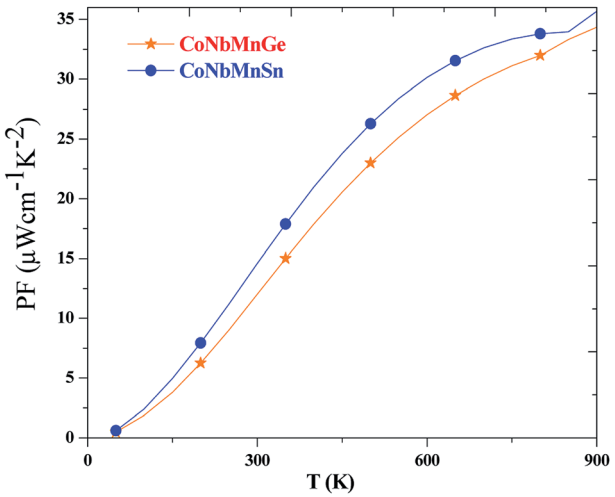


Fig. 12 The change in the power factor of CoNbMnZ (Z = Ge, Sn) with temperature.

## Conclusions

We have presented detailed information about the structural, electronic band structure, magnetic, elastic, and thermoelectric properties of CoNbMnZ (Z = Ge, Sn) alloys. Band structure analysis through GGA indicates that both alloys are metallic. However, upon the inclusion of mBJ, perfect half-metallic nature is observed, with indirect band gaps of 0.43 and 0.45 eV at the $\Gamma$- and $X$-points of the Brillouin zone. The states at the Fermi level are 100% spin polarized. The total magnetic moment per formula unit is 1 $\mu_B$, following the Slater–Pauling rule $M_T = Z_T - 24$. Charge density analysis reveals polar-covalent-type bonding. The mechanical stability is elucidated *via* calculating the elastic constants. Pugh's ratio, Poisson's ratio, and Cauchy's pressure values show the ductile nature of the alloys. The anisotropic factor value is more than 1, indicating that the properties are directionally dependent. Furthermore, the transport properties of CoNbMnZ (Z = Ge, Sn) reveal some interesting results. The value of $S$ shows an increasing trend over the whole temperature range, attaining maximum values of 60.43 and 68.20 for the alloys, and the positive value of $S$ predicts that holes are the majority carriers. The maximum power factor values are 32 and 35 at 900 K, also suggesting possible thermoelectric applications for these alloys.

## Conflicts of interest

The authors hereby declare that we have no conflict of interest.

## References

1 T. M. Bhat and D. C. Gupta, *J. Magn. Magn. Mater.*, 2017, **435**, 173.
2 S. Yousuf and D. C. Gupta, *J. Phys. Chem. Solids*, 2017, **108**, 109.
3 S. Yousuf and D. C. Gupta, *J. Alloys Compd.*, 2018, **735**, 1245.
4 S. A. Khandy and D. C. Gupta, *Semicond. Sci. Technol.*, 2017, **32**, 125019.
5 Y. Sutou, Y. Imano, N. Koeda, T. Omori, R. Kainuma, K. Ishidab and K. Oikawa, *Appl. Phys. Lett.*, 2004, **85**, 4358.
6 Z. Wen, T. Kubota, T. Yamamoto and K. Takanashi, *Sci. Rep.*, 2015, **5**, 18387.
7 S. Yousuf and D. C. Gupta, *Phys. B*, 2018, **534**, 5.
8 S. Yousuf and D. C. Gupta, *Indian J. Phys.*, 2017, **91**, 33.

9 L. Bainsla, M. M. Raja, A. K. Nigam and K. G. Suresh, *J. Alloys Compd.*, 2015, **651**, 631.
10 A. Kundu, S. Ghosh, R. Banerjee, S. Ghosh and B. Sanyal, *Sci. Rep.*, 2017, **7**, 1803.
11 R. A. de Groot, F. M. Mueller, P. G. van Engen and K. H. J. Buschow, *Phys. Rev. Lett.*, 1983, **50**, 2024.
12 X. Y. Dong, C. Adelmann, J. Q. Xie and C. J. Palmstrøma, *Appl. Phys. Lett.*, 2005, **86**, 102107.
13 V. Alijani, S. Ouardi, G. H. Fecher, J. Winterlik, S. S. Naghavi, X. Kozina, G. Stryganyuk, C. Felser, E. Ikenaga, Y. Yamashita, S. Ueda and K. Kobayashi, *Phys. Rev. B: Condens. Matter Mater. Phys.*, 2011, **84**, 224416.
14 L. Bainsla, A. I. Mallick, M. M. Raja, A. A. Coelho, A. K. Nigam, D. D. Johnson, A. Alam and K. G. Suresh, *Phys. Rev. B: Condens. Matter Mater. Phys.*, 2015, **92**, 045201.
15 L. Bainsla and K. G. Suresh, *Appl. Phys. Rev.*, 2016, **3**, 031101.
16 S. Singh and D. C. Gupta, *J. Alloys Compd.*, 2019, **806**, 1292.
17 T. M. Bhat and D. C. Gupta, *J. Electron. Mater.*, 2016, **45**, 6012.
18 F. Casper, T. Graf, S. Chadov, B. Balke and C. Felser, *Semicond. Sci. Technol.*, 2012, **27**, 063001.
19 T. Zhu, C. Fu, H. Xie, Y. Liu and X. Zhao, *Adv. Energy Mater.*, 2015, **5**, 1500588.
20 T. M. Tritt, H. Böttner and L. Chen, *MRS Bull.*, 2008, **33**, 366.
21 P. Ying, X. Liu, C. Fu, X. Yue, H. Xie, X. Zhao, W. Zhang and T. Zhu, *Chem. Mater.*, 2015, **27**, 909.
22 H. Zhu, J. Mao, Y. Li, J. Sun, Y. Wang, Q. Zhu, G. Li, Q. Song, J. Zhou, Y. Fu, R. He, T. Tong, Z. Liu, W. Ren, L. You, Z. Wang, J. Luo, A. Sotnikov, J. Bao, K. Nielsch, G. Chen, D. J. Singh and Z. Ren, *Nat. Commun.*, 2019, **10**, 270.
23 N. A. Koshi and R. John, *Eur. Phys. J. B*, 2019, **92**, 86.
24 J. P. Perdew, K. Burke and M. Ernzerhof, *Phys. Rev. Lett.*, 1996, **77**, 3868.
25 F. Tran and P. Blah, *Phys. Rev.*, 2009, **102**, 4.
26 G. K. H. Madsen and D. J. Singh, *Comput. Phys. Commun.*, 2006, **175**, 67.
27 B. Ryu and M. W. Oh, *J. Korean Ceram. Soc.*, 2016, **53**, 273.
28 S. Yousuf and D. C. Gupta, *J. Alloys Compd.*, 2018, **738**, 501.
29 T. Graf, C. Felser and S. S. P. Parkin, *Prog. Solid State Chem.*, 2011, **39**, 1.
30 T. M. Bhat and D. C. Gupta, *J. Electron. Mater.*, 2018, **47**, 2042.
31 Z. H. Liu, Y. J. Zhang, E. K. Liu, G. D. Liu, X. Q. Ma and G. H. Wu, *J. Phys. D: Appl. Phys.*, 2015, **48**, 1.
32 W. H. E. Schwarz, *J. Chem. Educ.*, 2010, **87**, 444.
33 T. M. Bhat and D. C. Gupta, *Mater. Res. Express*, 2017, **4**, 1.
34 S. A. Khandy and D. C. Gupta, *J. Phys. Chem. Solids*, 2019, **135**, 109079.
35 A. Reuss, *Z. Angew. Math. Mech.*, 1929, **9**, 49.
36 R. Hill, *J. Mech. Phys. Solids*, 1963, **11**, 375.
37 X. K. Liu, W. Zhou, Z. Zheng and S. M. Peng, *J. Alloys Compd.*, 2014, **615**, 975.
38 I. H. Bhat, T. M. Bhat and D. C. Gupta, *J. Phys. Chem. Solids*, 2018, **119**, 251.
39 S. A. Mir and D. C. Gupta, *J. Alloys Compd.*, 2020, **854**, 1–10.